Identifying Crystallization- and Incorporation-Limited Regimes during Vapor–Liquid–Solid Growth of Si Nanowires

Christopher W. Pinion, David P. Nenon, Joseph D. Christesen, and James F. Cahoon*

Department of Chemistry, University of North Carolina at Chapel Hill, Chapel Hill, North Carolina 27599-3290, United States

ABSTRACT The vapor–liquid–solid (VLS) mechanism is widely used for the synthesis of semiconductor nanowires (NWs), yet several aspects of the mechanism are not fully understood. Here, we present comprehensive experimental measurements on the growth rate of Au-catalyzed Si NWs over a range of temperatures (365–480 °C), diameters (30–200 nm), and pressures (0.1–1.6 Torr SiH_4). We develop a kinetic model of VLS growth that includes (1) Si incorporation into the liquid Au–Si catalyst, (2) Si evaporation from the catalyst surface, and (3) Si crystallization at the catalyst–NW interface. This simple model quantitatively explains growth rate data collected over more than 65 distinct synthetic conditions. Surprisingly, upon increasing the temperature and/or pressure, the analysis reveals an abrupt transition from a diameter-independent growth rate that is limited by incorporation to a diameter-dependent growth rate that is limited by crystallization. The identification of two distinct growth regimes provides insight into the synthetic conditions needed for specific NW-based technologies, and our kinetic model provides a straightforward framework for understanding VLS growth with a range of metal catalysts and semiconductor materials.

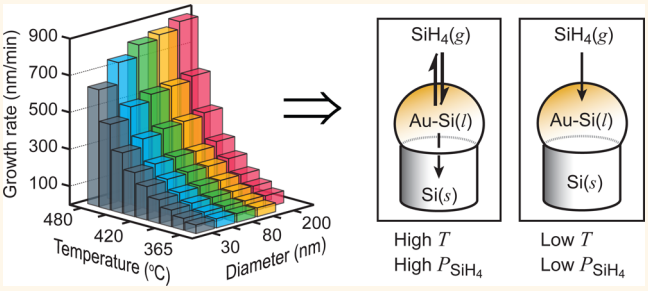

KEYWORDS: silicon nanowire · vapor–liquid–solid mechanism · Gibbs–Thomson effect · diameter-dependent growth rate

Semiconductor nanowires (NWs) have been widely explored as a fundamental building block of nanoscale devices[1,2] that can be used for optoelectronics,[3,4] photovoltaics,[5–8] and electronics.[9–11] NWs may be fabricated by a variety of methods,[12,13] and the vapor–liquid–solid (VLS) mechanism, originally proposed by Wagner and Ellis 50 years ago,[14–16] is often used for bottom-up NW synthesis. In the VLS process, vapor-phase semiconductor material is supplied to a metal catalyst, which forms a liquid alloy droplet because of a low eutectic temperature between the metal and semiconductor. For example, the eutectic temperature for Au and Si is ~363 °C (see the binary phase diagram in Figure 1A), enabling the formation of liquid droplets composed of ~20% Si above this temperature. During VLS growth, supersaturation of the liquid catalyst induces crystallization of the semiconductor material and elongation of the NW at the liquid–solid interface. These general aspects of the VLS mechanism are well-known; however, the microscopic kinetic and physical processes that determine the overall NW growth rate remain poorly understood and debated in the literature.

The VLS process has been demonstrated with a range of semiconductor materials including group IV Si,[14,15] Ge,[17] and group III–V GaAs,[18] GaN,[19] InP,[20] *etc.* materials as well as a range of metal catalysts including Au,[14,15] Ag,[21] Pt,[22,23] *etc.* For NW-based technologies, synthetic control of the VLS process has been used to control NW size,[24,25] composition,[18,26,27] and morphology[11,28–30] in order to encode specific functionality in the NW material. For group IV NWs, low-pressure chemical vapor deposition (CVD) with Au catalysts is often used for VLS growth in conjunction with hydride precursor gases such as silane (SiH_4), disilane (Si_2H_6), germane

* Address correspondence to jfcahoon@unc.edu.

Received for review March 11, 2014 and accepted May 9, 2014.

Published online May 09, 2014
10.1021/nn501403v

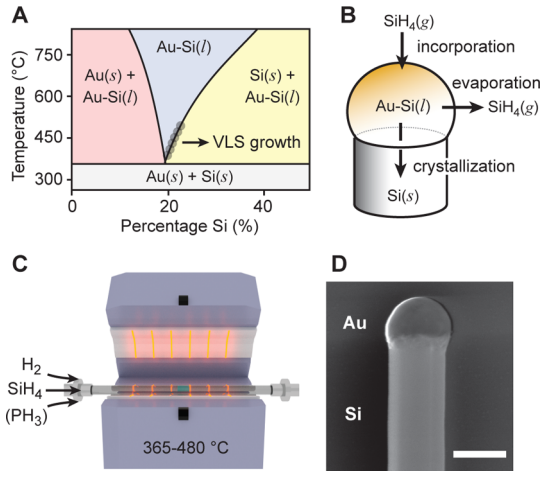

Figure 1. VLS growth of Si NWs by CVD. (A) Binary Au−Si phase diagram showing regions of solid Au, liquid Au−Si alloy, and solid Si as a function of weight percent Si. The approximate regions of the diagram accessed during the VLS growth are depicted by gray circles. (B) Illustration of the three key processes—incorporation, evaporation, and crystallization—that are used to model Si NW growth by the VLS mechanism. (C) Schematic of the hot-wall, low-pressure CVD system used for synthesis of Si NWs at temperatures of 365−480 °C. (D) SEM image of a Si NW grown using a ~150 nm diameter Au catalyst; scale bar, 150 nm.

(GeH_4), and digermane (Ge_2H_6). The relatively low decomposition temperatures of these precursors enable nucleation and growth of NWs by the VLS process at temperatures close to, or even below,[31] the eutectic temperature.

In this article, we discuss the VLS mechanism in the context of the three microscopic processes—incorporation, evaporation, crystallization—depicted in Figure 1B. The incorporation process encompasses dissociative adsorption of silane gas on the Au−Si liquid surface and incorporation of Si into the liquid catalyst. The evaporation process corresponds to the reverse reaction or associative desorption of silane gas from the Au−Si liquid surface. Finally, the crystallization process describes the nucleation of solid Si crystal planes at the liquid−solid interface, which irreversibly elongates the NW. We neglect diffusion in the Au−Si liquid catalyst because it is too rapid to be a rate-limiting step in small-diameter NWs[22,32] and also neglect diffusion of adsorbed Si on the substrate or NW surface, which has been shown to be of minimal importance for Si NW growth.[33] With a few exceptions,[34,35] reports on the kinetics of Si NW VLS growth generally do not include a Si evaporation or desorption process in the analysis. However, considering the principle of microscopic reversibility, there is no *a priori* rationale to exclude this reaction. In addition, evaporation from liquid alloy catalysts has previously been reported in the context of "negative whisker" formation—a process termed solid−liquid−vapor (SLV) etching because of its similarities to the VLS mechanism.[36,37]

The rate-limiting step for NW growth has been debated because experimental and theoretical reports have produced conflicting results.[17,22,23,32,33,38−41] For instance, Bootsma and Gassen observed a growth rate proportional to the partial pressure of silane and thus proposed an incorporation-limited mechanism.[17] More recently, Lew and Redwing reported similar results, also concluding that incorporation was the rate-limiting step.[32] In contradiction, Givargizov proposed a crystallization-limited mechanism because wires growing along different crystallographic directions exhibited different growth rates.[22]

Further information on the rate-limiting step is provided by the diameter dependence of the growth rate,[33,39] and it is widely agreed that either the curvature of the cylindrical NW or spherical catalyst droplet induces diameter dependence in the growth rate as a result of the Gibbs−Thomson effect.[22,35,39,40,42] Givargizov reported a decreasing growth rate with decreasing NW diameter, which he attributed to the Gibbs−Thomson effect reducing the catalyst chemical potential and thus the crystallization rate.[22] In a more recent study by Ross *et al.*, however, a diameter-independent growth rate was observed when using Si_2H_6 as the Si precursor at low pressures ($<10^{-5}$ Torr).[33] They concluded that VLS growth proceeds by an incorporation-limited mechanism. In addition, several recent theoretical studies have shown that the NW growth process involves coupled processes and cannot necessarily be reduced to a single rate-limiting step.[35,39]

To help resolve the long-standing ambiguities about the VLS growth process, we performed precise experimental measurements on the growth rate of Au-catalyzed Si NWs over a range of temperatures (365−480 °C), diameters (30−200 nm), and pressures (0.1−1.6 Torr SiH_4). NWs were synthesized in a hot-wall, quartz-tube CVD reactor (see schematic in Figure 1C) using silane as the Si precursor, phosphine (PH_3) for n-type doping with phosphorus, and hydrogen (H_2) as the carrier gas (see the Methods section for further details of NW growth). The NW diameter was controlled by the size of the Au catalysts deposited on growth substrates, and NWs are assumed to grow in the ⟨111⟩ direction, as reported previously.[25] The CVD apparatus and growth conditions used for our experiments are similar to those used widely within the NW community for group IV materials.[24,25,43,44] All synthetic conditions used in this study produce high-quality, single-crystalline NWs, as exemplified by the scanning electron microscopy (SEM) image in Figure 1D.

As shown in Figure 2, growth rate data were generated using a modification of our recently reported method, ENGRAVE (Encoded Nanowire GRowth and Appearance using VLS and Etching),[11] to sequentially encode n-type and intrinsic sections in the NWs at

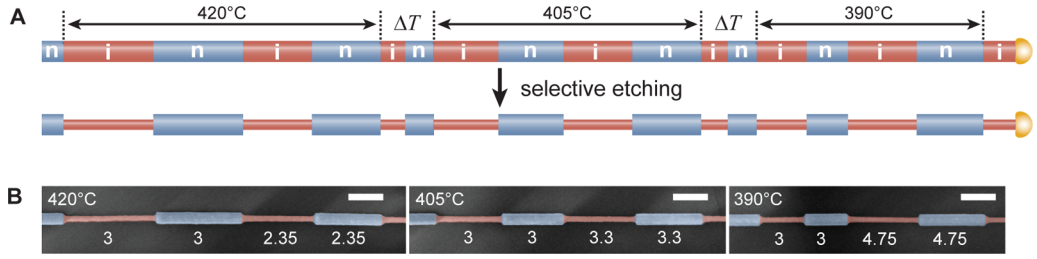

Figure 2. Determination of Si NW VLS growth rates using dopant modulation. (A) Top: Schematic illustration of alternating n-type (n) and intrinsic (i) segments encoded sequentially during VLS NW growth at temperatures of 420, 405, and 390 °C. Sections denoted ΔT are not drawn to scale and correspond to regions over which the temperature was lowered at a rate of 1 °C/min. Bottom: Illustration of the NW morphology that results from etching in aqueous KOH solution, which selectively removes intrinsic sections (red) of the NW. (B) False-colored SEM images of an ~80 nm diameter Si NW with sequential segments encoded at 420 (left), 405 (middle), and 390 °C (right). Growth times in minutes are denoted beneath each segment, and all segments were grown at a SiH_4 partial pressure of 0.4 Torr and total pressure of 40 Torr; scale bars, 250 nm. Analysis of these type of SEM images yielded quantitative temperature- and diameter-dependent growth rates.

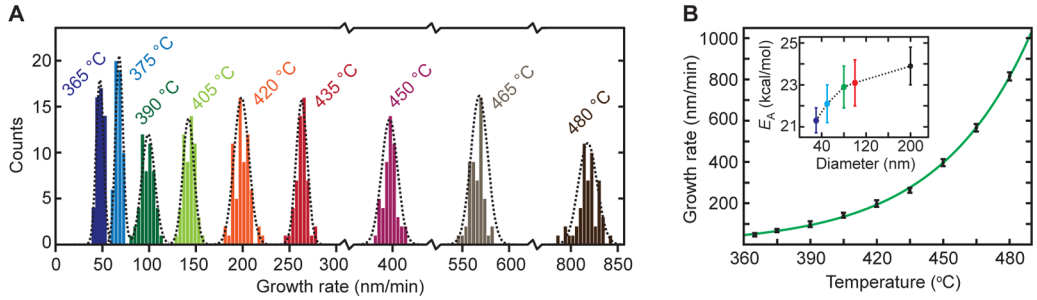

Figure 3. Temperature-dependent Si NW VLS growth rates. (A) Histogram of measured VLS growth rates acquired at temperatures ranging from 365 to 480 °C for NWs 80 nm in diameter at a SiH_4 partial pressure of 0.4 Torr. Dashed lines represent a fit of the data at each temperature to a Gaussian distribution. (B) Plot of growth rate *vs* temperature for the data contained in panel A; error bars reflect two standard deviations (2σ). The solid green line represents a fit to the Arrhenius expression. Inset: activation energy as a function of NW diameter, as determined by fits to growth rate data for NWs 30−200 nm in diameter.

various temperatures and SiH_4 partial pressures. Selective wet-chemical etching of the intrinsic sections (see Figure 2A) was used to reveal the length of individual sections, and quantitative SEM image analysis (see Figure 2B) yielded the measured growth rate for each section. For each unique combination of temperature, pressure, and diameter, more than 50 individual measurements of the growth rate were made across 10 or more NWs to ensure the statistical significance of the results. No significant difference in the growth rate of n-type and intrinsic sections was observed. This method has previously been used to measure Si NW growth rates in both VLS[11] and vapor−solid−solid (VSS)[45] mechanisms. Controlled axial modulation of composition or diameter has also been used to quantify the growth kinetics of $InP_{1-x}As_x$ NWs[46] and Ge NWs,[47] respectively.

RESULTS

Growth rate data collected at one diameter (80 nm) and one partial pressure (0.4 Torr SiH_4) for a range of temperatures are depicted as histograms in Figure 3A. The data at each temperature are well fit to a Gaussian distribution, producing a standard deviation of <8% of the average growth rate value. The dependence of growth rate on temperature (Figure 3B) is well fit to the Arrhenius expression, yielding an activation energy of 22.9 ± 1.0 kcal/mol that is in good agreement with literature values.[17,32,33,38,48,49] Similar analysis was performed for other diameters and partial pressures (see Supporting Information Figures S1 and S2). Interestingly, we observe a diameter-dependent activation energy (see inset Figure 3B), which, to our knowledge, has not been previously observed and is consistent with the enhanced catalytic activity observed with small-diameter noble metal nanoparticles.[50,51]

Growth rate data for diameters of 30−200 nm at a SiH_4 partial pressure of 0.4 Torr are displayed as a function of temperature in Figure 4A. For temperatures of 390 °C and below, we observed no statistically significant differences in the growth rates for NWs of different diameter. However, for temperatures of 435 °C and above, we observed definitively faster growth rates for larger-diameter NWs. Growth rate data are plotted as a function of NW diameter in Figure 4B. Low temperatures show no dependence on diameter, whereas higher temperatures show a nonlinear dependence, exhibiting growth rates that asymptotically increase with increasing diameter.

As shown in Figure 4C, we also examined the effect of SiH_4 partial pressure on the Si NW growth rate. The pressure-dependent growth rates are not linear over the full range of synthetic conditions examined—an

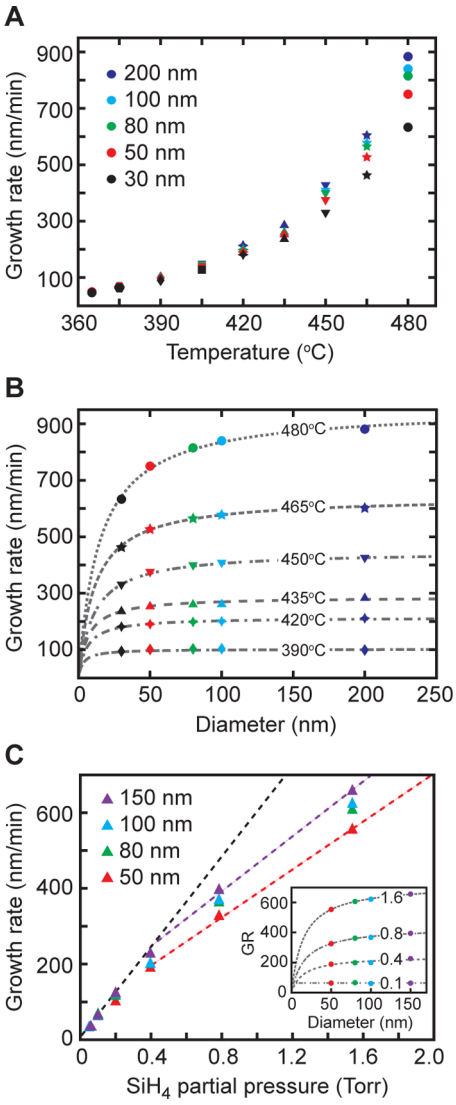

Figure 4. Diameter-dependent Si NW VLS growth rates. (A) Diameter-dependent growth rates as a function of temperature for Si NWs with diameters of 30 (black), 50 (red), 80 (green), 100 (blue), and 200 nm (indigo) at a SiH_4 partial pressure of 0.4 Torr. (B) NW growth rate as a function of diameter for temperatures of 390 (diamond), 420 (square), 435 (triangle), 450 (inverted triangle), 465 (star), and 480 °C (circle). Dashed lines represent a fit of the data at each temperature to eq 9 using two adjustable parameters, B and d_0. (C) NW growth rate as a function of silane partial pressure for NW diameters of 50 (red), 80 (green), 100 (blue), and 150 nm (purple). Dashed lines represent linear fits to the data. For partial pressures <0.3 Torr, all diameters were fit simultaneously (dashed black line). For partial pressures >0.3 Torr, the 150 nm (dashed purple) and 50 nm (dashed red) data were fit separately. Inset: NW growth rate (GR; nm/min) at 420 °C as a function of diameter for SiH_4 partial pressures ranging from 0.1 to 1.6 Torr. Dashed gray lines represent fits to eq 9. For panels A–C, error bars are comparable in size to the marker symbols and omitted for clarity.

observation in disagreement with previous studies that reported a purely linear dependence.[32,33] For the 420 °C data at low partial pressures (<0.2 Torr), the growth rate is diameter-independent but at higher partial pressures (>0.2 Torr) becomes diameter-dependent (see inset in Figure 4C). However, at 390 °C, the growth rate is diameter-independent for all SiH_4 partial pressures measured (see Figure S4).

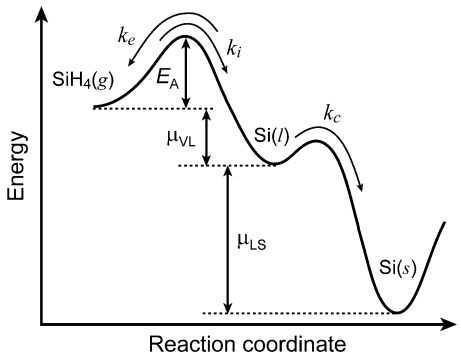

Figure 5. Kinetics and energetics of VLS NW growth. Energy landscape for the VLS mechanism, depicting the barriers and rate constants associated with incorporation, evaporation, and crystallization processes that govern the kinetics leading from gaseous SiH_4 to liquid AuSi to solid diamond-cubic Si.

KINETIC MODELING

To interpret the measured growth rate data, a kinetic analysis of VLS growth in the context of the three microscopic processes depicted in Figure 1B—incorporation, evaporation, and crystallization—is developed below. This analysis builds most directly on the work of Shakthivel and Raghavan.[35] An illustration of the kinetic processes and energy landscape for the VLS process in this analysis is depicted in Figure 5.

We consider a mechanism in which the incorporation step is reversible:

$$SiH_4(g) \underset{k_e}{\overset{k_i}{\rightleftharpoons}} Si(l) + 4H- \quad (1)$$

and the crystallization step is irreversible:

$$Si(l) \xrightarrow{k_c} Si(s) \quad (2)$$

where H– represents surface-adsorbed hydrogen, k_i the incorporation rate constant (units of s^{-1}), k_e the evaporation rate constant (units of $nm \cdot s^{-1}$), and k_c the crystallization rate constant (units of $nm \cdot s^{-1}$). The irreversible reaction in eq 2 implicitly assumes that the supersaturation of the Au–Si droplet and the liquid–solid chemical potential, μ_{LS}, are sufficiently high to irreversibly drive the crystallization process under all synthetic conditions. This assumption is supported by transmission electron microscopy studies of VLS NW growth, in which sequential deposition—but not dissolution—of Si crystal planes is observed under supersaturation conditions.[31,33]

A full analysis of eqs 1 and 2 under steady-state conditions, which includes the effects of surface-confined reactions at the liquid–vapor and liquid–solid interfaces (which introducing units of length to k_e and k_c), yields a NW growth rate, G, of (see Supporting Information for a full derivation):

$$G = \frac{k_c k_i}{k_e + k_c/2} \Omega \rho_{sites} K_{a/d} P \quad (3)$$

where Ω is the volume per atom for Si, $K_{a/d}$ is the silane adsorption/desorption equilibrium constant (units of inverse pressure), ρ_{sites} is the density of surface sites available for SiH_4 adsorption, and P is the partial pressure of SiH_4 in the reactor. Note the quantity $K_{a/d} \cdot P$ equals the fractional saturation, θ, of SiH_4 adsorption sites and would be expected to saturate (*i.e.*, $\theta = 1$) at sufficiently high P. Equation 3 also assumes that the NW and liquid droplet diameters are equal, introducing the factor of 1/2 in the denominator.

Each rate constant in eq 3 can potentially have dependencies on temperature and diameter. In this analysis, however, we assume that k_i is simply described by the Arrhenius expression, yielding the activation energies, E_A, depicted in the inset of Figure 3B. Although k_c may have a similar Arrhenius-type dependence on temperature that depends on the mechanism of crystallization,[35] we assume that the barrier to crystallization is substantially lower than the incorporation barrier[52] and thus neglect this temperature dependence for the temperature range examined in this study and treat k_c as a constant value.

The Gibbs–Thomson effect, which changes the chemical potential of Si within the catalyst droplet, appears through the dependence of k_e on NW diameter. The chemical potential difference between Si in the vapor and liquid phases, μ_{VL}, is given by[35]

$$\mu_{VL} = k_B T \ln\left(\frac{P}{P_0}\right) - k_B T \ln\left(\frac{C_{Si(l)}}{C_0}\right) - \frac{4\Omega\gamma_{VL}}{d} \quad (4)$$

where k_B is the Boltzmann constant, T is the temperature, P_0 is the vapor pressure of Si in the solid NW, $C_{Si(l)}$ is the concentration of Si in the supersaturated liquid droplet, C_0 is the equilibrium concentration of Si in the liquid droplet, γ_{VL} is the vapor–liquid surface tension of the droplet, and d is the diameter of the NW. The final term in eq 4, which scales as d^{-1}, accounts for the decrease of μ_{VL} as a result of the curved liquid surface, which is commonly referred to as the Gibbs–Thomson effect. As indicated by the plot in Figure 5, the energetic barrier for the evaporation process is the summation of E_A and μ_{VL}, yielding an Arrhenius-type expression for k_e of[35]

$$k_e = A \exp\left(\frac{-(E_A + \mu_{VL})}{kT}\right) \quad (5)$$

where A is a prefactor with units of nm·s^{-1}. Substituting eq 4 into eq 5 and simplifying to first order yields

$$k_e = A \exp\left(\frac{-E_A}{kT}\right)\left(\frac{P_0}{P}\right)\left(\frac{C_{Si(l)}}{C_0}\right)\exp\left(\frac{4\Omega\gamma_{VL}}{dkT}\right)$$
$$\approx A \exp\left(\frac{-E_A}{kT}\right)\left(\frac{P_0}{P}\right)\left(\frac{C_{Si(l)}}{C_0}\right)\left(1 + \frac{4\Omega\gamma_{VL}}{dkT}\right) \quad (6)$$

Therefore, k_e includes a d^{-1} dependence as a result of the Gibbs–Thomson effect. Note that we assume pseudo-first-order kinetics with respect to the adsorbed hydrogen concentration (*i.e.*, we assume a constant but unsaturated H coverage); thus, the prefactor in eq 6 includes a term proportional to the hydrogen coverage (see the Supporting Information).

Based on this analysis, two limits of eq 3 can be examined. First, for $k_c > 2k_e$, the growth rate becomes

$$G \approx 2k_i \Omega \rho_{sites} K_{a/d} P \quad (7)$$

and a diameter dependence is not expected as k_e does not appear in the expression. This limit can be considered an incorporation-limited regime because only k_i appears in the expression. Second, for the limit $k_c < 2k_e$, the growth rate becomes

$$G \approx \frac{k_i k_c}{k_e} \Omega K_{a/d} \rho_{sites} P = K_{eq} k_c \Omega K_{a/d} \rho_{sites} P \quad (8)$$

where $K_{eq} = k_i \cdot k_e^{-1}$ (units of nm^{-1}) is the equilibrium constant for incorporation/evaporation, and, as a result, the growth rate is dependent on diameter and scales as $(1 + 4\Omega\gamma_{VL}/dk_BT)^{-1}$. This limit can be considered a crystallization-limited regime because the slower rate of crystallization relative to incorporation/evaporation induces an equilibrium between incorporation/evaporation; consequently, the growth rate scales as $K_{eq} \cdot k_c$.

ANALYSIS AND DISCUSSION

The kinetic analysis presented above yields a diameter-independent, incorporation-limited regime (eq 7) and a diameter-dependent, crystallization-limited regime (eq 8). The key mechanistic aspects of each regime are illustrated in Figure 6A,B, respectively. By classifying our experimental data into these two regimes using the measured diameter dependence, we can generate the "phase" diagram depicted in Figure 6C, in which the incorporation-limited regime (red region) is observed at low temperatures and SiH_4 partial pressures and the crystallization-limited regime (green region) is observed at higher temperatures and pressures. There is a narrow window (blue region) over which we cannot conclusively discern the diameter dependence and thus cannot classify the growth regime.

The appearance of the incorporation-limited regime at low temperature is consistent with the limit ($2k_e < k_c$) taken for eq 7 because k_e is expected to be suppressed at lower temperatures as a result of the large energetic barrier, $E_A + \mu_{VL}$, for evaporation. Interestingly, at an intermediate temperature of 420 °C, we observe a transition from the incorporation-limited to crystallization-limited regime as the SiH_4 partial pressure increases. This observation is consistent with the results of Ross *et al.*,[33] in which an incorporation-limited and diameter-independent regime was observed for very low (<10^{-5} Torr) partial pressures at all temperatures. The transition observed here at higher (>0.2 Torr) partial pressures implies the limit $2k_e > k_c$ at higher

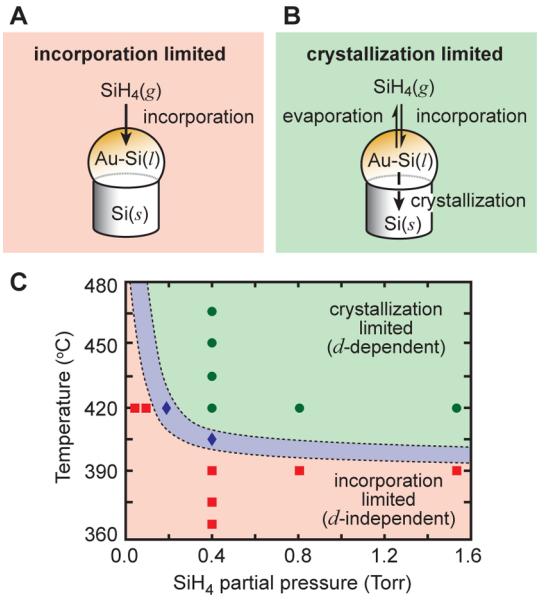

Figure 6. Identification of crystallization-limited and incorporation-limited regimes during VLS NW growth. (A) Illustration of the rate-determining kinetic processes for the incorporation-limited (diameter-independent) regime, which is dominated by the rate of Si incorporation from the gas phase. (B) Illustration of the rate-determining kinetic processes for the crystallization-limited (diameter-dependent) regime, which includes rapid gas−liquid equilibration and slower Si crystallization. (C) "Phase" diagram depicting regions of temperature and silane partial pressure in which VLS growth is crystallization-limited (shaded green), incorporation-limited (shaded red), or intermediate (shaded blue). Red squares denote synthetic conditions with a diameter-independent growth rate, green circles a diameter-dependent growth rate, and blue diamonds the transition between diameter-independent and diameter-dependent regimes. Boundaries between shaded regions are guides for the eye.

pressures. The dependence of k_e on partial pressure, P, is complex because the catalyst supersaturation and hydrogen surface coverage should both increase with P, potentially offsetting the P_0/P dependence in eq 6. This observation suggests the need for additional pressure-dependent studies in the transitional region shown in blue in Figure 6C to further understand the details of the processes that control the transition from diameter-independent to diameter-dependent regimes at constant temperature.

For data collected in the crystallization-limited regime, the diameter dependence of the growth rate can be fit using a simplification of eq 8 to

$$G \approx \frac{B}{1 + d_0/d} \qquad (9)$$

where $d_0 = 4\Omega\gamma_{VL}/k_BT$ (units of nm) and B is a proportionality constant. Fits of diameter-dependent data to this expression are shown in Figure 4B and reproduce the diameter-dependent increase in G with increasing NW diameter. Using the values for d_0 from these fits, we can estimate the vapor−liquid surface tension, γ_{VL}, yielding values of 0.7 ± 0.3, 0.8 ± 0.5, 1.3 ± 0.2, 1.4 ± 0.2, and 1.9 ± 0.5 J/m^2 for temperatures of 420, 435, 450, 465, and 480 °C, respectively. These values are in reasonably good agreement with reported values for liquid Si, 0.7−0.8 J/m^2,[53] and liquid Au, 1.0−1.2 J/m^2,[54] near their melting temperatures. The increasing γ_{VL} with temperature suggests that the liquid contact angle at the VLS triple junction should decrease with temperature.[55] SEM images of Au catalysts at 420 and 480 °C (see Figure S5) show a decrease in the contact angle by ~15°, following the trend observed with γ_{VL}. The large changes in γ_{VL} with temperature may suggest a change in composition of the AuSi liquid catalyst surface with temperature.[52,56]

The appearance of incorporation- and crystallization-limited regimes also explains the nonlinear dependence of growth rate on partial pressure that is apparent in Figure 4C. An examination of eqs 7 and 8 shows that the slopes of growth rate *versus* pressure should be different in the two regimes. Separate fits of the pressure-dependent data for partial pressures below 0.3 Torr (dashed black) and above 0.3 Torr (dashed purple and dashed red lines) are shown in Figure 4C, and approximately linear behavior is observed in both regimes. Furthermore, above 0.3 Torr, data from smaller-diameter NWs exhibits a lower slope (red dashed line) relative to larger NWs (purple dashed line). This result is predicted by eq 8 because k_e increases with smaller diameters, reducing the slope for small-diameter NWs in the crystallization-limited regime.

CONCLUSIONS

We performed comprehensive measurements of the Si NW VLS growth rate over a range of temperatures, pressures, and diameters that are widely used for development of NW-based technologies using CVD synthesis. By developing a kinetic analysis that includes the microscopic processes of incorporation, evaporation, and crystallization, NW growth was classified into a diameter-dependent, crystallization-limited regime and diameter-independent, incorporation-limited regime. Analysis of the experimental growth rate data revealed the incorporation regime to dominate at low temperatures and pressures, whereas the crystallization-limited regime dominates at higher temperatures and pressures. The growth regime changes over a surprisingly narrow region of temperature and pressure during CVD growth.

In addition to fundamental insights on the mechanism of the VLS process, our analysis may be used to choose the synthetic conditions needed for specific technological applications. For instance, if NWs of uniform length but different diameters are required, the incorporation-limited regime is appropriate. However, if NWs with abrupt axial transitions are needed, such as for heterostructures, the crystallization-limited regime is more appropriate because the liquid−vapor equilibrium will facilitate fast exchange of material in the liquid catalyst.

Finally, we expect crystallization-limited and incorporation-limited regimes to be accessible for a range of semiconductor precursors and metal catalysts, although the growth conditions needed to reach these regimes may be specific to each system. For instance, the group IV hydride precursors GeH_4, Si_2H_6, and Ge_2H_6 exhibit a lower activation barrier for decomposition than the SiH_4 precursor used in this study.[31,57,58] Facile decomposition of the precursor would favor equilibrium between incorporation and evaporation (see Figure 6B). As a result, the diameter-dependent, crystallization-limited regime would be expected to persist to lower temperatures and partial pressures than observed in this study. In agreement with this prediction, a recent study of Ge NW growth kinetics using the GeH_4 precursor reported diameter-dependent growth rates as low as 300 °C.[47] Nevertheless, a sufficiently low partial pressure of the precursor would still be expected to yield a diameter-independent, incorporation-limited regime. For example, diameter-independent growth kinetics were observed with Si_2H_6 at temperatures as high as 650 °C but under extremely low partial pressure, high-vacuum conditions.[33] Thus, the analysis presented in this study appears to reconcile several conflicting reports in the literature, and we expect the insights into VLS growth discussed in this article to be applicable to a range of NW systems.

METHODS

Nanowire Growth. Si NWs were grown by a VLS mechanism in a home-built, hot-wall CVD system using Au nanoparticles as catalysts, SiH_4 (Voltaix) as the source of Si, PH_3 (Voltaix; diluted to 1000 ppm in H_2) as the source of P for n-type doping, and H_2 (Matheson TriGas 5N semiconductor grade) as the carrier gas. The CVD system has been described in detail elsewhere.[11] For a typical NW growth run, citrate-stabilized Au catalysts (BBI International) of the indicated diameter were dispersed on 1 × 2 cm Si wafers (University Wafer; p-type Si with 600 nm thermal oxide) that had been functionalized with poly-L-lysine solution (Aldrich). These growth substrates were inserted into the center of a 1 in. diameter quartz tube furnace (Lindberg Blue M), and the furnace temperature was ramped to 450 °C to nucleate NW growth for 5 min using 2.00 sccm SiH_4 and 200.0 sccm H_2 at 40.0 Torr total reactor pressure. Note that the reactor pressure and all partial pressures noted in the text correspond to external, room-temperature measurements of the pressure. The reactor temperature was altered in a stepwise manner as described in the text (see Figure 2A). To prevent disruption of the NW growth, all changes in temperature were performed at a rate of 1 °C/min. Similarly, changes in SiH_4 partial pressure were performed by incrementally altering the SiH_4 flow in sequential steps that increased the partial pressure by a factor of 2 or less. All n-type segments were encoded using a PH_3 flow rate needed to achieve a SiH_4/PH_3 gas-phase ratio of 400:1 or less.

Image Analysis. SEM imaging was performed with an FEI Helios 600 Nanolab dual beam system with an imaging resolution of less than 5 nm. The length of each n-type or intrinsic segment was determined from SEM images using home-written MATLAB image analysis software. An edge-finding algorithm was used to extract the NW diameter as a function of axial position, and the n-type/intrinsic boundary (*e.g.*, from left to right in Figure 2) was defined as the onset of a decrease in diameter. The subsequent intrinsic/n-type boundary was defined as the onset of an increase in diameter. We estimate the uncertainty in segment length to be ±5 nm from repeated imaging and analysis of the same segments. The growth rate was calculated from the measured segment length and the growth time. The diameter of each NW (defined as the diameter of the Si wire at the base of the Au catalyst) was also measured in order to bin NWs into diameters of 30, 50, 80, 100, 150, and 200 nm corresponding to measured diameter ranges of 25−35, 45−55, 75−85, 95−105, 140−160, and 190−210 nm, respectively.

Conflict of Interest: The authors declare no competing financial interest.

Acknowledgment. This work was wholly funded by the National Science Foundation through Grant DMR-1308695. We thank D. Hill, T. Celano, C. Flynn, and X. Zhang for useful discussions and help with figure preparation. We also thank the staff of the Chapel Hill Analytical and Nanofabrication Laboratory (CHANL) user facility for assistance with NW imaging.

Supporting Information Available: Details of the kinetic analysis, Arrhenius plots for NWs of different diameter, histograms of growth rate data for all synthetic conditions, discussion of critical diameter, partial pressure dependence of growth rates at 390 °C, and data tables of measured growth rates for all diameter, temperature, and partial pressure combinations. This material is available free of charge *via* the Internet at http://pubs.acs.org.

REFERENCES AND NOTES

1. Lieber, C. M. Semiconductor Nanowires: A Platform for Nanoscience and Nanotechnology. *MRS Bull.* **2011**, *36*, 1052–1063.
2. Yang, P.; Yan, R.; Fardy, M. Semiconductor Nanowire: What's Next? *Nano Lett.* **2010**, *10*, 1529–1536.
3. Law, M.; Sirbuly, D. J.; Johnson, J. C.; Goldberger, J.; Saykally, R. J.; Yang, P. Nanoribbon Waveguides for Subwavelength Photonics Integration. *Science* **2004**, *305*, 1269–1273.
4. Qian, F.; Li, Y.; Gradečak, S.; Wang, D.; Barrelet, C. J.; Lieber, C. M. Gallium Nitride-Based Nanowire Radial Heterostructures for Nanophotonics. *Nano Lett.* **2004**, *4*, 1975–1979.
5. Zhang, X.; Pinion, C. W.; Christesen, J. D.; Flynn, C. J.; Celano, T. A.; Cahoon, J. F. Horizontal Silicon Nanowires with Radial p−n Junctions: A Platform for Unconventional Solar Cells. *J. Phys. Chem. Lett.* **2013**, *4*, 2002–2009.
6. Tian, B.; Kempa, T. J.; Lieber, C. M. Single Nanowire Photovoltaics. *Chem. Soc. Rev.* **2009**, *38*, 16–24.
7. Kempa, T. J.; Day, R. W.; Kim, S.-K.; Park, H.-G.; Lieber, C. M. Semiconductor Nanowires: A Platform for Exploring Limits and Concepts for Nano-enabled Solar Cells. *Energy Environ. Sci.* **2013**, *6*, 719–733.
8. Hochbaum, A. I.; Yang, P. Semiconductor Nanowires for Energy Conversion. *Chem. Rev.* **2010**, *110*, 527–546.
9. Lee, S. H.; Jung, Y.; Agarwal, R. Highly Scalable Non-volatile and Ultra-Low-Power Phase-Change Nanowire Memory. *Nat. Nanotechnol.* **2007**, *2*, 626–630.
10. Yao, J.; Yan, H.; Das, S.; Klemic, J. F.; Ellenbogen, J. C.; Lieber, C. M. Nanowire Nanocomputer as a Finite-State Machine. *Proc. Natl. Acad. Sci. U.S.A.* **2014**, *111*, 2431–2435.
11. Christesen, J. D.; Pinion, C. W.; Grumstrup, E. M.; Papanikolas, J. M.; Cahoon, J. F. Synthetically Encoding 10 nm Morphology in Silicon Nanowires. *Nano Lett.* **2013**, *13*, 6281–6286.
12. Dick, K. A. A Review of Nanowire Growth Promoted by Alloys and Non-alloying Elements with Emphasis on Au-Assisted III−V Nanowires. *Prog. Cryst. Growth Charact. Mater.* **2008**, *54*, 138–173.

13. Peng, K.-Q.; Lee, S.-T. Silicon Nanowires for Photovoltaic Solar Energy Conversion. *Adv. Mater.* **2011**, *23*, 198–215.
14. Wagner, R. S.; Ellis, W. C. Vapor–Liquid–Solid Mechanism of Single Crystal Growth. *Appl. Phys. Lett.* **1964**, *4*, 89–90.
15. Wagner, R. S.; Ellis, W. C. Vapor–Liquid–Solid Mechanism of Crystal Growth and Its Application to Silicon. *Trans. Metall. Soc. AIME* **1965**, *233*, 1053–1064.
16. Wagner, R. S.; Ellis, W. C.; Jackson, K. A.; Arnold, S. M. Study of the Filamentary Growth of Silicon Crystals from the Vapor. *J. Appl. Phys.* **1964**, *35*, 2993–3000.
17. Bootsma, G. A.; Gassen, H. J. A Quantitative Study on the Growth of Silicon Whiskers from Silane and Germanium Whiskers from Germane. *J. Cryst. Growth* **1971**, *10*, 223–234.
18. Gudiksen, M. S.; Lauhon, L. J.; Wang, J.; Smith, D. C.; Lieber, C. M. Growth of Nanowire Superlattice Structures for Nanoscale Photonics and Electronics. *Nature* **2002**, *415*, 617–620.
19. Huang, Y.; Duan, X.; Cui, Y.; Lieber, C. M. Gallium Nitride Nanowire Nanodevices. *Nano Lett.* **2002**, *2*, 101–104.
20. Duan, X.; Huang, Y.; Cui, Y.; Wang, J.; Lieber, C. M. Indium Phosphide Nanowires as Building Blocks for Nanoscale Electronic and Optoelectronic Devices. *Nature* **2001**, *409*, 66–69.
21. Wittemann, J. V.; Münchgesang, W.; Senz, S.; Schmidt, V. Silver Catalyzed Ultrathin Silicon Nanowires Grown by Low-Temperature Chemical-Vapor-Deposition. *J. Appl. Phys.* **2010**, *107*, 096105.
22. Givargizov, E. I. Fundamental Aspects of VLS Growth *J. Cryst. Growth* **1975**, *31*, 20–30.
23. Weyher, J. Some Notes on the Growth Kinetics and Morphology of VLS Silicon Crystals Grown with Platinum and Gold as Liquid-Forming Agents. *J. Cryst. Growth* **1978**, *43*, 235–244.
24. Cui, Y.; Lauhon, L. J.; Gudiksen, M. S.; Wang, J. F.; Lieber, C. M. Diameter-Controlled Synthesis of Single-Crystal Silicon Nanowires. *Appl. Phys. Lett.* **2001**, *78*, 2214–2216.
25. Wu, Y.; Cui, Y.; Huynh, L.; Barrelet, C. J.; Bell, D. C.; Lieber, C. M. Controlled Growth and Structures of Molecular-Scale Silicon Nanowires. *Nano Lett.* **2004**, *4*, 433–436.
26. Yang, C.; Zhong, Z. H.; Lieber, C. M. Encoding Electronic Properties by Synthesis of Axial Modulation-Doped Silicon Nanowires. *Science* **2005**, *310*, 1304–1307.
27. Bjork, M. T.; Ohlsson, B. J.; Sass, T.; Persson, A. I.; Thelander, C.; Magnusson, M. H.; Deppert, K.; Wallenberg, L. R.; Samuelson, L. One-Dimensional Steeplechase for Electrons Realized. *Nano Lett.* **2002**, *2*, 87–89.
28. Tian, B.; Xie, P.; Kempa, T. J.; Bell, D. C.; Lieber, C. M. Single-Crystalline Kinked Semiconductor Nanowire Superstructures. *Nat. Nanotechnol.* **2009**, *4*, 824–829.
29. Crawford, S.; Lim, S. K.; Gradecak, S. Fundamental Insights into Nanowire Diameter Modulation and the Liquid/Solid Interface. *Nano Lett.* **2013**, *13*, 226–232.
30. Lim, S. K.; Crawford, S.; Haberfehlner, G.; Gradecak, S. Controlled Modulation of Diameter and Composition along Individual III–V Nitride Nanowires. *Nano Lett.* **2013**, *13*, 331–336.
31. Kodambaka, S.; Tersoff, J.; Reuter, M. C.; Ross, F. M. Germanium Nanowire Growth below the Eutectic Temperature. *Science* **2007**, *316*, 729–732.
32. Lew, K.-K.; Redwing, J. M. Growth Characteristics of Silicon Nanowires Synthesized by Vapor–Liquid–Solid Growth in Nanoporous Alumina Templates. *J. Cryst. Growth* **2003**, *254*, 14–22.
33. Kodambaka, S.; Tersoff, J.; Reuter, M. C.; Ross, F. M. Diameter-Independent Kinetics in the Vapor–Liquid–Solid Growth of Si Nanowires. *Phys. Rev. Lett.* **2006**, *96*, 096105.
34. Dubrovskii, V. G.; Sibirev, N. V. General Form of the Dependences of Nanowire Growth Rate on the Nanowire Radius. *J. Cryst. Growth* **2007**, *304*, 504–513.
35. Shakthivel, D.; Raghavan, S. Vapor–Liquid–Solid Growth of Si Nanowires: A Kinetic Analysis. *J. Appl. Phys.* **2012**, *112*, 024317.
36. Givargizov, E. I.; Babasian, R. A. Mechanisms and Kinetics of Vapor-Phase Etching of GaAs and GaP. *J. Electron. Mater.* **1980**, *9*, 883–904.
37. Kim, B. J.; Stach, E. A. Desorption Induced Formation of Negative Nanowires in GaN. *J. Cryst. Growth* **2011**, *324*, 119–123.
38. Kikkawa, J.; Ohno, Y.; Takeda, S. Growth Rate of Silicon Nanowires. *Appl. Phys. Lett.* **2005**, *86*, 123109.
39. Schmidt, V.; Senz, S.; Gösele, U. Diameter Dependence of the Growth Velocity of Silicon Nanowires Synthesized *via* the Vapor–Liquid–Solid Mechanism. *Phys. Rev. B* **2007**, *75*, 045335.
40. Dubrovskii, V.; Sibirev, N.; Cirlin, G.; Soshnikov, I.; Chen, W. H.; Larde, R.; Cadel, E.; Pareige, P.; Xu, T.; Grandidier, B.; *et al.* Gibbs–Thomson and Diffusion-Induced Contributions to the Growth rate of Si, InP, and GaAs Nanowires. *Phys. Rev. B* **2009**, *79*, 205316.
41. Dubrovskii, V. G.; Sibirev, N. V.; Cirlin, G. E. Kinetic Model of the Growth of Nanodimensional Whiskers by the Vapor–Liquid–Crystal Mechanism. *Technol. Phys. Lett.* **2004**, *30*, 682–686.
42. Dubrovskii, V. G. Refinement of the Wagner–Ellis Formula for the Minimum Radius and the Givargizov–Chernov Formula for the Growth Rate of Nanowire. *Technol. Phys. Lett.* **2013**, *39*, 157–160.
43. Allen, J. E.; Hemesath, E. R.; Perea, D. E.; Lensch-Falk, J. L.; Li, Z. Y.; Yin, F.; Gass, M. H.; Wang, P.; Bleloch, A. L.; Palmer, R. E.; *et al.* High-Resolution Detection of Au Catalyst Atoms in Si Nanowires. *Nat. Nanotechnol.* **2008**, *3*, 168–173.
44. Bjork, M. T.; Schmid, H.; Knoch, J.; Riel, H.; Riess, W. Donor Deactivation in Silicon Nanostructures. *Nat. Nanotechnol.* **2009**, *4*, 103–107.
45. Cohen-Karni, T.; Casanova, D.; Cahoon, J. F.; Qing, Q.; Bell, D. C.; Lieber, C. M. Synthetically Encoded Ultrashort-Channel Nanowire Transistors for Fast, Pointlike Cellular Signal Detection. *Nano Lett.* **2012**, *12*, 2639–2644.
46. Harmand, J. C.; Glas, F.; Patriarche, G. Growth Kinetics of a Single $InP_{1-x}As_x$ Nanowire. *Phys. Rev. B* **2010**, *81*, 235436.
47. Musin, I. R.; Shin, N.; Filler, M. A. Diameter Modulation as a Route To Probe the Vapour–Liquid–Solid Growth Kinetics of Semiconductor Nanowires. *J. Mater. Chem. C* **2014**, *2*, 3285–3291.
48. Schmid, H.; Björk, M. T.; Knoch, J.; Riel, H.; Riess, W.; Rice, P.; Topuria, T. Patterned Epitaxial Vapor–Liquid–Solid Growth of Silicon Nanowires on Si(111) Using Silane *J. Appl. Phys.* **2008**, *103*, 024304.
49. Schmidt, V.; Wittemann, J. V.; Gosele, U. Growth, Thermodynamics, and Electrical Properties of Silicon Nanowires. *Chem. Rev.* **2010**, *110*, 361–388.
50. Haruta, M. When Gold Is Not Noble: Catalysis by Nanoparticles. *Chem. Rec.* **2003**, *3*, 75–87.
51. Tsunoyama, H.; Sakurai, H.; Negishi, Y.; Tsukuda, T. Size-Specific Catalytic Activity of Polymer-Stabilized Gold Nanoclusters for Aerobic Alcohol Oxidation in Water. *J. Am. Chem. Soc.* **2005**, *127*, 9374–9375.
52. Wang, H.; Zepeda-Ruiz, L. A.; Gilmer, G. H.; Upmanyu, M. Atomistics of Vapour–Liquid–Solid Nanowire Growth. *Nat. Commun.* **2013**, *4*, 1956.
53. Millot, F.; Sarou-Kanian, V.; Rifflet, J. C.; Vinet, B. The Surface Tension of Liquid Silicon at High Temperature. *Mater. Sci. Eng., A* **2008**, *495*, 8–13.
54. Lide, D. R. *CRC Handbook of Chemistry and Physics*, 72nd ed.; CRC Press: Boca Raton, FL, 1991.
55. Roper, S. M.; Anderson, A. M.; Davis, S. H.; Voorhees, P. W. Radius Selection and Droplet Unpinning in Vapor–Liquid–Solid-Grown Nanowires. *J. Appl. Phys.* **2010**, *107*, 114320.
56. Shpyrko, O. G.; Streitel, R.; Balagurusamy, V. S.; Grigoriev, A. Y.; Deutsch, M.; Ocko, B. M.; Meron, M.; Lin, B.; Pershan, P. S. Surface Crystallization in a Liquid AuSi Alloy. *Science* **2006**, *313*, 77–80.
57. Park, W. I.; Zheng, G.; Jiang, X.; Tian, B.; Lieber, C. M. Controlled Synthesis of Millimeter-Long Silicon Nanowires with Uniform Electronic Properties. *Nano Lett.* **2008**, *8*, 3004–3009.
58. Deleglise, F.; Dutartre, D.; Rubaldo, L.; Talbot, A.; Fellous, C. Si-SiGe(C) Epitaxy by RTCVD. In *Silicon Heterostructure Handbook*; Cressler, J. D., Ed.; CRC Press: Boca Raton, FL, 2005; pp 45–83.